Microstructure of epitaxial $Ba_{0.7}Sr_{0.3}TiO_3/SrRuO_3$ bilayer films on $SrTiO_3$ substrates

J. Q. He,[a] E. Vasco,[b] C. L. Jia, and R. Dittmann
Institut für Festkörperforschung, Forschungzentrum Jülich GmbH, D-52425 Jülich, Germany

R. H. Wang
Department of Physics and Center for Electron Microscopy, Wuhan University, Wuhan 430072, People's Republic of China

(Received 23 November 2004; accepted 1 March 2005; published online 3 May 2005)

The thickness evolution of the microstructure of epitaxial $Ba_{0.7}Sr_{0.3}TiO_3$ thin films grown on $SrRuO_3/SrTiO_3$ was investigated by means of transmission electron microscopy. Within the $Ba_{0.7}Sr_{0.3}TiO_3$ layer, a layered structure (three sublayers) is distinguished as for the configuration of lattice strain and defects. The first sublayer extends for 3 nm from the lattice-coherent $Ba_{0.7}Sr_{0.3}TiO_3/SrRuO_3$ interface. The second 13-nm-thick sublayer forms a semicoherent interface with the first sublayer due to the creation of a misfit dislocation network. The third sublayer extends beyond the second sublayer exhibiting a structure characterized by compact columnar features. Planar defects are formed at the boundaries between such features. The formation of a layered structure within the $Ba_{0.7}Sr_{0.3}TiO_3$ films is discussed in the light of the growth modes of films on lattice-mismatched substrates. © *2005 American Institute of Physics*. [DOI: 10.1063/1.1897067]

I. INTRODUCTION

$Ba_{0.7}Sr_{0.3}TiO_3$ (BST) has attracted a lot of attention in recent years as a high-permittivity material for high-density dynamic random access memory (DRAM) capacitors[1–5] as well as material with dielectric properties tunable through its composition (i.e., Ba/Sr ratio)[6] for microwave devices operating at room temperature. Whereas permittivities in the order of 10 000 are achieved for BST in bulk form,[7] the dielectric response of BST thin films is strongly suppressed, the ferroelectric-to-paraelectric phase transition is significantly broadened,[8] and a collapse of the dielectric response is observed as the film thickness decreases. The latter effect is often attributed to low-permittivity layers at the BST/electrode interfaces. Since defect network close to the interface may be the origin of such low-permittivity layers, the study of the near-interface regions by transmission electron microscopy (TEM) constitutes an ahead step towards the understanding of the dielectric properties of BST thin films. It has been demonstrated that bulklike permittivities and comparable sharp phase transitions can be obtained in all-oxide epitaxial $SrRuO_3$ (SRO)/BST/SRO capacitors.[9] However, the compressive strain ($\approx -1\%$) imposed on epitaxial BST thin films by the bottom electrode and/or substrate, as well as the resulting misfit dislocations, exerts a critical influence on their dielectric properties.[9–13] For example, the inhomogeneous stress field associated with threading dislocations has been discussed as possible mechanism for the dielectric degradation, e.g., the broadening of the phase transition in BST thin films.[14,15] Whereas BST films with thicknesses in the order of 20 nm have been reported to grow in a two-dimensional way,[9] thicker films are reported to have a columnar structure with a thickness-dependent grain size which has been connected with thickness dependence of the dielectric response.[16] Therefore, the evolution of the microstructure with increasing thickness is an issue of crucial importance for the engineering of BST thin-film-based devices.

In this work, we present a detailed analysis of the crystalline quality and the microstructure of BST thin films epitaxially grown on $SrRuO_3/SrTiO_3$ (STO). The evolution of the film microstructure with its thickness is investigated by cross-sectional high-resolution TEM (HRTEM). A strong thickness dependence of the x-ray diffraction (XRD) and Rutherford backscattering spectroscopy (RBS) data corroborates the HRTEM observations. Furthermore, a detailed analysis of the local lattice distortion provides insights into the in-plane and out-of-plane strain distribution in BST thin films. On the basis of the experimental results a growth model of BST films on SRO is proposed for different thickness regimes.

II. EXPERIMENTAL PROCEDURE

This films were prepared on commercial single-crystalline (001) STO substrates. The BST/SRO heterostructures were grown *in situ* by pulsed laser deposition (PLD), employing a KrF excimer laser ($\lambda = 248$ nm) with an energy density of 5 J/cm^2 and a pulse frequency of 10 Hz. Bottom SRO layers with thickness of 100 nm were deposited at 775 °C in the presence of an oxygen dynamic pressure of 25 Pa. The surface of these layers was free of the strain originating from the SRO/STO interface. Subsequently, the BST films were grown at a deposition temperature of 680 °C and the same oxygen pressure. The BST film thicknesses were in the range of 4–210 nm. Finally, 30-nm-thick SRO

[a]Author to whom correspondence should be addressed; present address: Department of Biology, Brookhaven National Laboratory, 50 Bell Ave. Upton, NY 11973; electronic mail: jhe@bnl.gov
[b]Present address: Instituto de Ciencia de Materiales de Madrid, Consejo Superior de Investigaciones Científicas, 28049 Cantoblanco, Madrid, Spain.

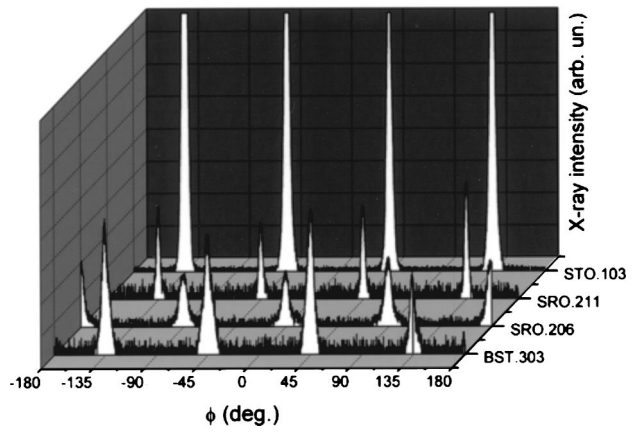

FIG. 1. XRD ϕ-scan of the STO 103, SRO 211, SRO 206, and BST 303 peaks indicating a [001]BST∥[110/001]SRO∥[001]STO epitaxial relationship.

layers were deposited as top electrode on some of the previously grown samples of BST/SRO/STO under the deposition conditions used for bottom SRO layers.

Cross-sectional specimens for TEM observation were prepared by cutting the film-covered wafer into slices. Two of the slices were glued together face to face and embedded in epoxy resin. After the glue was cured, disks with a diameter of 3 mm were obtained by cutting away excess epoxy. These disks were then ground, dimpled, polished, and subsequently Ar-ion milled in a stage cooled with liquid nitrogen. TEM and HRTEM investigations were performed in a JEOL 4000EX microscope.

III. RESULTS

The epitaxial relationship of BST and SRO on STO was proved by XRD ϕ-scan measurements, as shown in Fig. 1 [001] BST is ∥[001]STO via two SRO out-of-plane orientations; [110]SRO∥[001]STO and 45°-rotated cube-on-cube [001]SRO∥[001]STO, which are formed by two in-plane arrangements each. Rocking curves with a full width of 0.05° at half maximum of the BST 002 peak were measured for BST/SRO and SRO/BST/SRO heterostructures. Figure 2 shows the RBS spectra [random (□) and channeling (○)] of SRO/BST/SRO heterostructures with different BST thicknesses (a) 9, (b) 16, and (c) 43 nm. While the 9- and 16-nm-thick samples exhibit minimum channeling yields ($\chi = 1.6\% - 1.8\%$) extremely low indicating very low densities of lattice defects, the 43-nm-thick sample shows a relatively high yield ($\chi = 7.5\%$), which is attributable to a moderate defect density. These evidences give us a hint on the thickness dependence of defect density in the analyzed heterostructures.

To clarify the origin of the above observations, the microstructure of the BST films was investigated by TEM and HRTEM. Figure 3(a) shows a cross-sectional image of a 4-nm-thick BST film stacked between two SRO layers. This film is strained by the SRO layers through the coherent BST/SRO interfaces. No misfit dislocations were observed in the 4-nm-thick BST film. As the BST film thickness increases (>9 nm), misfit dislocations are observed and their density rises. In addition, a layered structure appears in the bulk of

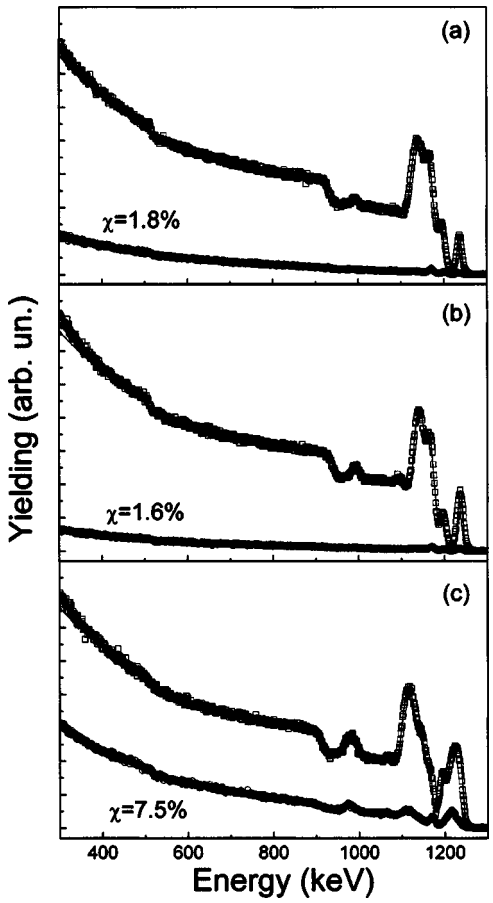

FIG. 2. 1.4-MeV He^{++} RBS random (□) and channeling (○) spectra of 9-nm- (a), 16-nm- (b), and 43-nm- (c) thick BST films deposited on 100-nm SRO/STO. The symbols represent the experimental data whereas the solid lines correspond to the simulated spectra. The minimum channeling yields (χ) are specified.

BST films thicker than 9 nm. Figures 3(b) and 3(c) show the lattice images of 9- and 30-nm-thick BST films, respectively. The horizontal arrows denote the BST/SRO interfaces whereas the dot lines indicate the inner interface between BST sublayers. As shown in Figs. 3(b) and 3(c), the first sublayer extends for 3 nm from the lattice-coherent BST/SRO interface. The morphology and thickness of this first sublayer are independent of the thicknesses of the subsequent sublayers. The second sublayer is separated from the first one by a network of misfit dislocations and has a thickness of about 13 nm [Fig. 3(c)]. The third sublayer exhibits a columnar structure characterized by the presence of planar defects [as pointed by the vertical arrows in Fig. 3(c)], which arises from the interface with second sublayer. These defects are mostly formed at the boundary of columnar features, and few of them propagate into the second sublayer.

The 210-nm-thick BST film shows a similar microstructure to that of the 30-nm-thick film shown in Fig. 3(c). However, the density of misfit dislocations at the interface between the first sublayer and the second sublayer in the 210-nm-thick film is higher than that in the 30-nm-thick film. Figure 4 shows a lattice image (with [001] BST as out-of-plane direction) of the near-interface region of the 210-nm-thick BST sample. The vertical arrows indicate three misfit dislocations *A*, *B*, and *C* with Burgers vectors

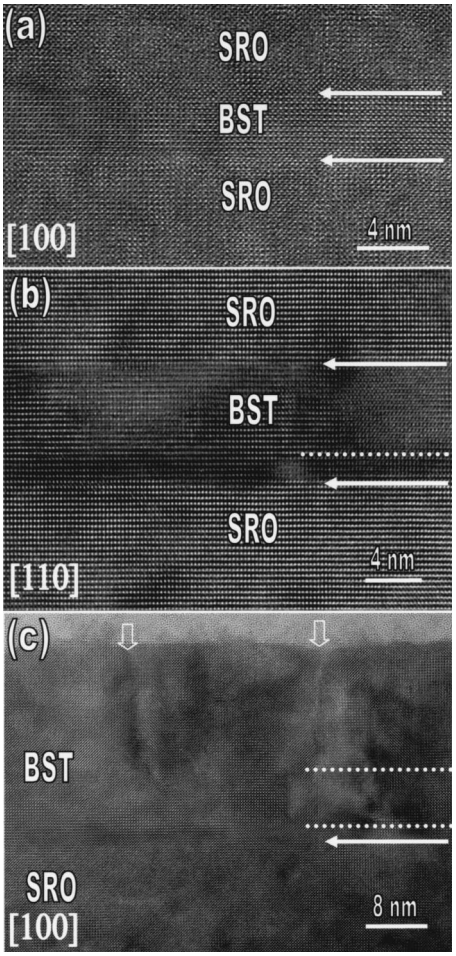

FIG. 3. Low-magnification lattice fringe images of 4-nm- (a), 9-nm- (b), and 30-nm- (c) thick BST films stacked between 30-nm- (top) and 100 -nm- (bottom) thick SRO layers. The horizontal arrows denote the SRO/BST and BST/SRO interfaces, the dot lines mark the sublayer interfaces, and the vertical arrows point to planar defects between columnar features. Zone axis is indicated in the left bottom of each image.

$a/2[110]$, $a[010]$, and $a/2[\bar{1}10]$, respectively. Two of them are accompanied by planar defects, which run into the second sublayer. The possible residual mismatch strain in the 210-nm-thick film was estimated from the periodic separation and the Burgers vector of these misfit dislocations. We obtained a value of 27 nm for the average spacing between $a\langle 010\rangle$ dislocations. The measured spacing is larger than that expected (i.e., 24 nm) for a fully relaxed BST film via the generation of $a\langle 010\rangle$ misfit dislocations indicating the presence of residual mismatch strain in the BST film. The residual strain was also confirmed by electron-diffraction analysis that shows diffraction spots more clearly split along the out-of-plane direction than those along in-plane directions (not shown here).

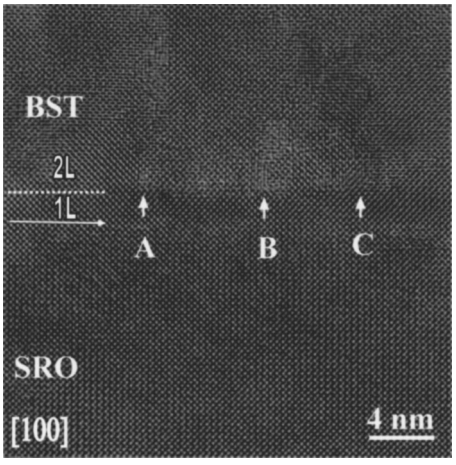

FIG. 4. Lattice image of 210-nm-thick BST film shows three dislocations *A*, *B*, and *C* with Burger vectors of $a/2[110]$, $a[010]$, and $a/2[\bar{1}10]$, respectively, at the interface between the first 2.7-nm-thick sublayer (1L) and the second sublayer (2L).

Figure 5(a) shows a lattice image of a 17-nm-thick film. The interfaces between the BST film and the top and bottom SRO layers are marked by the two horizontal arrows. A perfect misfit dislocation is marked by a vertical arrowhead. The lattice distortion and strain along the out-of-film plane axis ($\parallel$[001] BST) were investigated by geometric phase analysis.[17] The analysis reveals that the lattice distortion magnitude in the BST film changes anisotropically with the distance from the dislocation core. Figure 5(b) shows the map of lattice distortion along the out-of-plane axis [i.e., $S_\perp = (\langle a_{\mathrm{SRO}}\rangle - c_{\mathrm{BST}})/c_{\mathrm{BST}}$, a_{SRO} and c_{BST} being the out-of-plane lattices of SRO and BST, respectively] within the region imaged in Fig. 5(c). The difference of contrast corresponds to different distortion levels. Thus, the BST-layered structure is prominently displayed in Fig. 5(b) (as discussed below) due to different levels of remaining strain in each sublayer. Figures 5(c) and 5(d) plot the profiles of the lattice distortion $S_\perp$ in a dislocation core area and a dislocation-free area, respectively. These profiles were obtained by scanning the enclosed areas in Fig. 5(b) in the arrow direction from the upper SRO/BST interface and averaging horizontally $S_\perp$ ($\parallel$[010] BST) for each film depth within the frames. The profiles indicate that the lattice distortion induced by the misfit strain in the first sublayer [region 1L in Figs. 5(c) and 5(d)] is higher than that of the second sublayer (region 2L). In addition, the profiles reveal that the relaxation of the lattice strain via the formation of misfit dislocations occurs preferentially along the out-of-plane directions so that the regions seated directly above the dislocations show a lattice distortion lower than that of the interdislocation regions. Such an anisotropic relaxation mechanism gives rise to a nonuniform strain distribution in the upper SRO/BST interface.

IV. DISCUSSION

The above results on the BST-layered structure can be understood in terms of a change of the growth mode during the film deposition. In the lattice-mismatched BST/SRO system, the BST thin film grows coherently on the SRO surface starting from a two-dimensional (2D) nucleation process taking place at early growth stages. Initially, the lattice mismatch in the system is accommodated via lattice strain and/or perturbations in the surface of the growing film [e.g., by inducing local curvatures, periodic one-dimensional (1D)/2D structures such as dots and ripples, or just modifying the surface roughness]. The lattice-coherent film becomes unstable with the increase of its thickness due to the

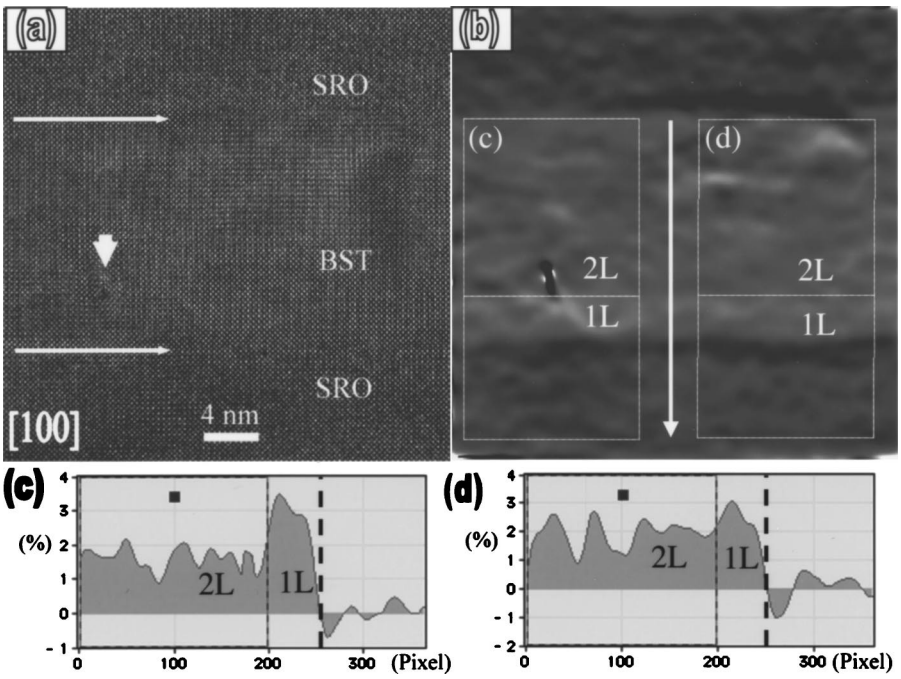

FIG. 5. (a) Lattice images of a 17 -nm-thick BST film stacked between 30-nm- (top) and 100-nm- (bottom) thick SRO layers. (b) Map of the lattice distortion along the out-of-plane axis (∥[001]BST) within region displayed in (a). The frames are used to average horizontally the lattice distortion map, so-obtained profiles in arrow direction are shown in (c) and (d). The depth axes correspond to the vertical distance to the upper SRO/BST interface measured in pixel. Profiles of the lattice distortion relative to the SRO lattice within dislocation core (c) and dislocation-free (d) areas. 1L and 2L denote the first and second BST sublayers.

energy collected by the mismatch strain. Once the thickness exceeds a critical value at which the strain-associated energy becomes higher than that required for the formation of misfit dislocations the film relaxes partially through the creation of such dislocations giving rise to a reduction of the system energy. On the one hand the misfit dislocations relieve the global mismatch strain, but on the other hand they introduce local lattice distortions and break down the homogeneity of the strain field within the volume of the semicoherent film. During this growth stage, the number of the created dislocations is still insufficient for a full relaxation of the mismatch strain. Thus, the film regions seated directly above the dislocations are more relaxed than those between dislocations (as demonstrated by the strain field map in Fig. 5). As the film thickness increases, the density of misfit dislocations, which continues being insufficient to the local system relaxation, rises. This incomplete strain relief induces a second relaxation mechanism: a columnar growth regime. The inhomogeneity of the strain field within the film bulk produces a nonuniform distribution of mismatch strain in the film surface with relaxed areas surrounded by strained areas. Such a distribution favors the heterogeneous nucleation and coarsening of three-dimensional (3D) islands on the relaxed areas, where the nucleation energy is lower. The number of nucleated 3D islands increases as the crossover to the columnar growth regime shifts toward larger thickness. The defects accumulated in the coalescence regions of the islands can easily induce the planar defects observed by TEM whereas the nondislocation-free volume of the developed 3D islands would correspond to the columnar features detected in the film bulk. This argument is coherent with the results obtained from RBS analysis (see Fig. 1), which shows that for BST films thicker than 16 nm the density of defects (i.e., misfit dislocations and planar defects) increases rapidly with the increasing thickness. Thus, the rapid increase of the defect density can be understood on the basis of the dynamics of growth and coalescence of the islands and the formation of a high density of misfit dislocations. From TEM and RBS results, a clear growth mode of strained BST as a function of the film thickness can be depicted:[18] (i) Up to a thickness of 3 nm, the BST film grows coherently on SRO surface starting from a 2D nucleation process. (ii) Up to 13 nm, BST film grows semicoherently exhibiting few misfit dislocations. (iii) The partially relaxed surface of the semicoherent film induces a columnar growth regime of 3D islands for thicker films with the formation of planar defects between islands and a high density of misfit dislocations inside the islands.

The BST growth mode proposed here gives rise to an anisotropic strain relaxation, which could provide a feasible explanation for the broadening of the ferroelectric-to-paraelectric phase transition observed in BST thin films as film thickness decreases. Furthermore, our results indicate that a continuous decrease of the strain with increasing thickness, which describes in a reliable way the thickness dependence of the lattice parameters and the dielectric properties of BST films thicker than 50 nm[9] should fail for thinner films as the first sublayer remains strained. Thus, if the influence of the strain is not superposed by other dominant electrode-related effects (e.g., incomplete screening of the electrodes), a discontinuity of the dielectric properties is expected for film thicknesses in the range of 15 nm where the transition from 2D to 3D growth occurs.

V. CONCLUSIONS

Our detailed analysis reveals the layered microstructure of epitaxial BST thin films stacked between SRO layers. A model is proposed on the basis of the TEM and RBS results to describe the evolution of the growth mode of BST films with the thickness from 2D layer-by-layer to 3D columnar growth (as predicted by the Stransky–Krastanov theory). Strain analysis shows an inhomogeneous mismatch strain field within the BST film bulk along the out-of-plane direc-

tion (different sublayers) and along the in-plane directions as well. This strain field structure may provide a feasible explanation for the broadening of the ferroelectric-to-paraelectric phase transition as widely observed in BST films thinner than 50 nm.

[1]H. J. Gao, C. L. Chen, B. Rafferty, S. J. Pennycook, G. P. Luo, and C. W. Chu, Appl. Phys. Lett. **75**, 2542 (1999).
[2]Q. X. Jia, X. D. Wu, S. R. Foltyn, and P. Tiwari, Appl. Phys. Lett. **66**, 2197 (1995).
[3]S. Y. Kuo and W. F. Hsieh, Phys. Rev. B **64**, 224103 (2001).
[4]K. Abe, J. Ceram. Soc. Jpn. **109**, S58 (2001).
[5]K. Abe, N. Yanase, K. Sano, M. Izuha, N. Fukushima, and T. Kawakubo, Integr. Ferroelectr. **21**, 197 (1998).
[6]W. J. Kim, H. D. Wu, W. Chang, S. B. Qadri, J. M. Pond, S. W. Kirchoefer, D. B. Chrisey, and J. S. Horwitz, J. Appl. Phys. **88**, 5448 (2000).
[7]A. D. Hilton and B. W. Ricketts, J. Phys. D **29**, 1321 (1996).
[8]C. Basceri, S. K. Streiffer, A. I. Kingon, and R. Waser, J. Appl. Phys. **82**, 2497 (1997).
[9]R. Dittmann, E. Vasco, R. Plonka, N. A. Pertsev, J. Q. He, C. L. Jia, S. Hoffmann-Eifert, and R. Waser, Appl. Phys. Lett. **83**, 5011 (2003).
[10]N. A. Pertsev, A. G. Zembilgotov, and A. K. Tagantsev, Phys. Rev. Lett. **80**, 1988 (1998).
[11]H. Li, A. L. Roytburd, S. P. Alpay, T. D. Tran, L. Salamanca-Riba, and R. Ramesh, Appl. Phys. Lett. **78**, 2354 (2001).
[12]J. Q. He, E. Vasco, C. L. Jia, R. Dittmann, and R. H. Wang, Appl. Phys. Lett. (submitted).
[13]B. H. Park, E. J. Peterson, Q. X. Jia, J. Lee, X. Zeng, W. Si, and X. X. Xi, Appl. Phys. Lett. **78**, 533 (2001).
[14]C. L. Canedy, H. Li, S. P. Alpay, L. Salamanca-Riba, A. L. Roytburd, and R. Ramesh, Appl. Phys. Lett. **77**, 1695 (2000).
[15]I. B. Misirlioglu, A. L. Vasiliev, M. Aindow, and S. P. Alpay, Appl. Phys. Lett. **84**, 1742 (2004).
[16]L. J. Sinnamon, M. M. Saad, R. M. Bowman, and J. M. Gregg, Appl. Phys. Lett. **81**, 703 (2002).
[17]M. J. Hytch, E. Snoeck, and R. Kilaas, Ultramicroscopy **74**, 131 (1998).
[18]J. C. Jiang and X. Q. Pan, J. Appl. Phys. **89**, 6365 (2001).